First Results from the Taiwan Axion Search Experiment with Haloscope at $20\,\mu\mathrm{eV}/c^{2*}$

Ann Author[†] and Second Author[‡]

Authors' institution and/or address

*This line break forced with *

(TASEH Collaboration)

(Dated: January 14, 2022)

Abstract

This paper presents the first results from the Taiwan Axion Search Experiment with Haloscope, a search for axions using a microwave cavity at frequencies between 4.707506 and 4.798145 GHz. Apart from external signals, no candidates with significance more than $3.355\,\sigma$ were found. The experiment excludes models with the axion-two-photon coupling $g_{a\gamma\gamma} \gtrsim zzzz \times 10^{-13}\,\mathrm{GeV}^{-1}$, a factor of ten above the benchmark KSVZ model for the mass range $xxxx < m_a < yyyy\,\mu\mathrm{eV}/c^2$. For the first time, constraints on the $g_{a\gamma\gamma}$ have been placed in this mass region.

CONTENTS

---

* A footnote to the article title

† Also at Physics Department, XYZ University.

‡ Second.Author@institution.edu

I.   INTRODUCTION

The axion is a hypothetical particle predicted as a consequence of a solution to the strong CP problem [1–3], i.e. why the product of the charge conjugation (C) and parity (P) symmetries is preserved in the strong interactions when there is an explicit CP-violating term in the QCD Lagrangian. In other words, why is the electric dipole moment of the neutron so tiny: $|d_n| < 1.8 \times 10^{-26}\ e \cdot \mathrm{cm}$ [4, 5]? The solution proposed by Peccei and Quinn is to introduce a new global Peccei-Quinn $U(1)_{PQ}$ symmetry that is spontaneously broken; the axion is the pseudo Nambu-Goldstone boson of $U(1)_{PQ}$ [1]. Axions are abundantly produced during the QCD phase transition in the early universe and may constitute the dark matter (DM). In the post-inflationary PQ symmetry breaking scenario, where the PQ symmetry is broken after inflation, current calculations suggest a mass range of 1—100 $\mu\mathrm{eV}/c^2$ for axions so that the cosmic axion density does not exceed the observed cold DM density [6–18]. Refs [19–21] also suggested that axions form a Bose-Einstein condensate; this property explains the occurrence of caustic rings in galactic halos. Therefore, axions are compelling because they may explain at the same time puzzles that are on scales different by more than thirty orders of magnitude.

Axions could be detected and studied via their two-photon interaction, the so-called "inverse Primakoff effect". For QCD axions, i.e. the axions proposed to solve the strong CP problem, the axion-two-photon coupling constant $g_{a\gamma\gamma}$ is related to the mass of the axion m_a:

$$g_{a\gamma\gamma} = \left(\frac{g_\gamma \alpha}{\pi \Lambda^2} \right) m_a, \tag{1}$$

where g_γ is a dimensionless model-dependent parameter, α is the fine-structure constant, $\Lambda = 78$ MeV is a scale parameter that can be derived from the mass and the decay constant of the pion, and the ratio of the up to down quark masses. The numerical values of g_γ are -0.97 and 0.36 in the Kim-Shifman-Vainshtein-Zakharov (KSVZ) [22, 23] and the Dine-Fischler-Srednicki-Zhitnitsky (DFSZ) [24, 25] benchmark models, respectively.

The detectors with the best sensitivities to axions with a mass of $\approx \mu\text{eV}/c^2$, as first put forward by Sikivie [26, 27], are haloscopes consisting of a microwave cavity immersed in a strong static magnetic field and operated at a temperature below 0.1 K. In the presence of an external magnetic field, the ambient oscillating axion field induces an electric current that oscillates with a frequency ν set by the total energy of the axion: $h\nu = E_a = m_a c^2 + \frac{1}{2} m_a v^2$. The induced electric current and the microwave cavity act as coupled oscillators and resonate when the frequencies of the electromagnetic modes in the cavity match ν; the signal power is further delivered in the form of microwave photons and readout with a low-noise amplifier. The axion mass is unknown, therefore, the cavity resonator must allow the possibility to be tuned through a range of possible axion masses. Over the years, the Axion Dark Matter eXperiment (ADMX) had developed and improved the cavity design and readout electronics and excluded KSVZ benchmark model within the mass range of 1.9–4.2 $\mu\text{eV}/c^2$ and DFSZ benchmark model for the mass range of 2.66–3.31 $\mu\text{eV}/c^2$ [28–34]. The Haloscope at Yale Sensitive to Axion Cold dark matter (HAYSTAC) [35] and the Center for Axion and Precision Physics Research (CAPP) [36] aim for axions at higher masses and have pushed the limits on $g_{a\gamma\gamma}$ towards the KSVZ value for the mass ranges of 16.96–17.12 and 17.14–17.28 $\mu\text{eV}/c^2$, and 10.7126–10.7186 $\mu\text{eV}/c^2$, respectively. This paper presents the first results and the analysis details of a search for axions for the mass range of $xxxx$–$yyyy$ $\mu\text{eV}/c^2$, from the Taiwan Axion Search Experiment with Haloscope (TASEH).

A.   The expected axion signal power and signal line shape

The signal power extracted from a microwave cavity on resonance is given by:

$$P_s = \left(g_\gamma^2 \frac{\alpha^2 \hbar^3 c^3 \rho_a}{\pi^2 \Lambda^4} \right) \times \left(\omega_c \frac{1}{\mu_0} B_0^2 V C_{mnl} Q_L \frac{\beta}{1+\beta} \right), \tag{2}$$

where $\rho_a = 0.45 \text{ GeV/cm}^3$ is the local dark-matter density. The second set of parentheses contains parameters related to the experimental setup: the angular resonance frequency of the cavity ω_c, the vacuum permeability μ_0, the average strength of the external magnetic field B_0, the volume of the cavity V, and the loaded quality factor of the cavity $Q_L = Q_0/(1+\beta)$, where Q_0 is the unloaded, intrinsic quality factor of the cavity and β determines the amount of coupling of the signal to the receiver. The form factor C_{mnl} is the normalized overlap of the electric field $\vec{\mathbf{E}}$, for a particular cavity resonant mode, with the external magnetic field

$\vec{\mathbf{B}}$:

$$C_{mnl} = \frac{\left[\int \left(\vec{\mathbf{B}} \cdot \vec{\mathbf{E}}_{mnl}\right) d^3\mathbf{x}\right]^2}{B_0^2 V \int E_{mnl}^2 d^3\mathbf{x}}. \tag{3}$$

Here, the magnetic field $\vec{\mathbf{B}}$ points mostly along the axial direction (z-axis) of the cavity. The field strength has a small variation along the radial and axial directions and B_0 is the averaged value over the whole cavity volume. For cylindrical cavities, the largest form factor is from the TM_{010} mode. The expected signal power derived from the experimental parameters of TASEH (see Table I) is $P_s \simeq 1.5 \times 10^{-24}$ W for a KSVZ axion with a mass of $19.5\,\mu eV/c^2$.

In the direct dark matter search experiments, several assumptions were made in order to derive a signal line shape. The density and the velocity distributions of DM are related to each other through the gravitational potential. The DM in the galactic halo is assumed to be virialized. The DM halo density distribution is assumed to be spherically symmetric and close to be isothermal, which results in a velocity distribution similar to the Maxwell-Boltzmann distribution. The distribution of the measured signal frequency can be further derived from the velocity distribution after a change of variables and set $h\nu_a = m_a c^2$. Previous experimental results typically adopt the following function for frequency $\nu \geq \nu_a$:

$$f(\nu) = \frac{2}{\sqrt{\pi}}\sqrt{\nu - \nu_a}\left(\frac{3}{\alpha}\right)^{3/2} e^{\frac{-3(\nu - \nu_a)}{\alpha}}, \tag{4}$$

where $\alpha \equiv \nu_a \langle v^2 \rangle / c^2$ and is related to the variance of the velocity distribution. For the Maxwell-Boltzmann distribution, $\langle v^2 \rangle = 3 v_c^2/2 = (270$ km/s$)^2$ where $v_c = 220$ km/s is the local circular velocity of DM in the galactic rest frame. Equation (4) is modified if one considers that the relative velocity of the DM halo with respect to the Earth is not the same as the DM velocity in the galactic rest frame [37]. The velocity distributions shall also be truncated so that the DM velocity is not larger than the escape velocity of the Milky Way [38]. Several N-body simulations [39, 40] follow structure formation from the initial DM density perturbations to the largest halo today and take into account the merger history of the Milky Way, rather than assuming that the Milky Way is in a steady state; the simulated results suggest velocity distributions with more high-speed particles relative to the Maxwellian case [41, 42]. However, these numerical simulations contain only DM particles; an inclusion of baryons may enhance the halo's central density due to a condensation of gas towards the center of the halo via an adiabatic contraction [43, 44], or may reduce the

5

density due to the supernova outflows, etc [45, 46].

In order to compare the results of TASEH with those of the former experiments, the analysis presented in this paper assumes an axion signal line shape by including Eq. (4) in the weights when merging the measured power from multiple frequency bins (see Section IV). Still given the caveats above and a lack of strong evidence for any particular choice of velocity distributions, the results without an assumption of signal line shape and the results with a simple Gaussian weight are also presented for comparison. In addition, a signal line width $\Delta\nu_a = m_a \langle v^2 \rangle /h \simeq 5$ kHz, which is much smaller than the TASEH cavity line-width $\nu_a/Q_L \simeq 250$ kHz, is assumed and five frequency bins are merged to perform the final analysis. For a signal line shape as described in Eq. (4), a 5-kHz bandwidth includes about 95% of the distribution.

B. The expected noise and the signal-to-noise ratio

Several physics processes can contribute to the total noise and all of them can be seen as Johnson thermal noise at some effective temperature, or the so-called system noise temperature T_{sys}. The total noise power in a bandwidth $\Delta\nu$ is then:

$$P_n = k_B T_{\mathrm{sys}} \Delta\nu, \tag{5}$$

where k_B is the Boltzmann constant. The system noise temperature T_{sys} has three major components:

$$k_B T_{\mathrm{sys}} = h\nu \left(\frac{1}{e^{h\nu/k_B T_{\mathrm{cavity}}} - 1} + \frac{1}{2} \right) + k_B T_A. \tag{6}$$

The three terms in Eq. (6) correspond to the blackbody radiation from the cavity at temperature T_{cavity}, the quantum noise associated with the zero-point fluctuation of the blackbody gas, and the noise added by the receiver. The first term in Eq. (6) implies that the noise spectrum from the cavity has little dependence on the frequency (white spectrum) for the narrow bandwidth considered in the experiment. However, the noise spectrum observed by TASEH was actually Lorentzian due to the temperature difference between the cavity and the transmission line in the dilution refrigerator. More details may be found in Section II and Appendix A.

Using the operation parameters of TASEH in Table I and the results from the calibration of readout electronics, the effective temperatures of these three sources are estimated to be

6

about 0.07 K, 0.12 K, and $1.9 - 2.2$ K, respectively. Therefore, the value of T_{sys} for TASEH is about 2.1–2.4 K, which gives a noise power of approximately $(1.5 - 1.7) \times 10^{-19}$ W for a bandwidth of 5 kHz (the assumed axion signal line-width), three orders of magnitude larger than the signal. Nevertheless, what matters in the analysis is the signal significance, or the so-called signal-to-noise ratio (SNR) using the standard terminology of axion experiments, i.e. the ratio of the signal power to the uncertainty in the estimation of the noise power:

$$\mathrm{SNR} = \frac{P_s}{\delta P_n} = \frac{P_s}{P_n} \sqrt{\Delta \nu_a \tau},$$

$$= \frac{P_s}{k_B T_{sys}} \sqrt{\frac{\tau}{\Delta \nu_a}}, \tag{7}$$

where τ is the amount of data integration time. Equation (7) can be derived from Dicke's Radiometer Equation, assuming that the amplitude distribution of the noise voltage within a bandwidth $\Delta \nu_a$ is Gaussian.

II. EXPERIMENTAL SETUP

The detector of TASEH is located at the Department of Physics, National Central University, Taiwan and housed within a cryogen-free dilution refrigerator (DR) from BlueForcs. A 8-Tesla superconducting solenoid with a bore diameter of 76 mm and a length of 240 mm is integrated with the DR.

The data for the analysis presented in this paper were collected by TASEH from October 13, 2021 to November 15, 2021, and termed as the CD102 data. During the data taking, the cavity sat in the center of the magnet bore and was connected via holders to the mixing chamber plate of the DR at a temperature of $\approx$30 mK. Due to an inefficiency of thermal conduction and thermal radiation, the temperature of the cavity stayed at 155 mK, higher with respect to the DR. The cavity, made of oxygen-free high-conductivity (OFHC) copper, has an effective volume of 0.234 L and is a two-cell cylinder split along the axial direction (z-axis). The cylindrical cavity has an inner radius of 2.5 cm and a height of 12 cm. In order to maintain a smooth surface, the cavity underwent the processes of polishing, chemical cleaning, and annealing. The resonance frequency of the TM_{010} mode can be tuned over the range of 4.717–4.999 GHz via the rotation of an off-axis OFHC copper tuning rod, from the position closer to the cavity wall to the position closer to the cavity center. The CD102 data cover the frequency range of 4.707506–4.798145 GHz. There were 839 frequency steps

7

¹⁷⁷ in total, with a frequency difference of 95–115 kHz between the steps. The form factor C_{010}

¹⁷⁸ as defined in Eq. (3) varies from 0.64 to 0.69 over the full frequency range. The intrinsic,

¹⁷⁹ unloaded quality factor Q_0 at the cryogenic temperature ($T_{\text{cavity}} \simeq 155$ mK) is $\simeq 60000$ at

¹⁸⁰ the frequency of 4.74 GHz.

¹⁸¹ An output probe, made of a 50-Ω semi-rigid coaxial cable soldering SMA plug crimp,

¹⁸² was inserted into the cavity and its depth was set for $\beta \simeq 2$. The signal from the output

¹⁸³ probe was directed to an impedance-matched amplification chain. The first-stage amplifier

¹⁸⁴ was a low noise high-electron-mobility transistor (HEMT) amplifier with an effective noise

¹⁸⁵ temperature of ≈ 2 K, mounted on the 4K-flange. The signal was further amplified at room

¹⁸⁶ temperature via a a three-stage post-amplifier, and down-converted and demodulated to

¹⁸⁷ in-phase (I) and quadrature (Q) components and digitized by an analog-to-digital converter

¹⁸⁸ (ADC) with a sampling rate of 2 MHz. The frequency resolution of the spectra was 1 kHz.

¹⁸⁹ A more detailed description of the TASEH detector, the operation of the data run, and

¹⁹⁰ the calibration of the gain and added noise temperature of HEMT can be found in Ref. [**?**

¹⁹¹]. See Table I for the benchmark experimental parameters that can be used to estimate the

¹⁹² sensitivity of TASEH.

¹⁹³ **III. THE CALIBRATION OF HEMT**

¹⁹⁴ The first stage of the amplification chain is HEMT, whose added noise dominates the noise

¹⁹⁵ from the readout electronics and could be expressed in terms of an effective temperature T_A

¹⁹⁶ (see Section I B). The noise is one of the most important parameters for the axion searches.

¹⁹⁷ Therefore, calibration for the HEMT is a crucial part in the operation of TASEH. In order

¹⁹⁸ to perform a calibration, the HEMT was connected to a heat source (resistors) instead of

¹⁹⁹ the cavity; various values of input currents were sent to the source to change its temperature

²⁰⁰ monitored by a thermometer. The power from the source was delivered following the same

²⁰¹ transmission line as that in the axion data running: first to the HEMT, then to the amplifiers

²⁰² outside the DR at room temperature, and finally to the signal analyzer. The received power

²⁰³ was fitted to a first-order polynomial, as a function of the source temperature, to extract the

²⁰⁴ gain and added noise for the HEMT. More details of the procedure can be found in Ref. [**?**

²⁰⁵].

²⁰⁶ The calibration was carried out before, during, and after the data taking, which showed

8

TABLE I. The benchmark experimental parameters for estimating the sensitivity of TASEH. The definitions of the parameters can be found in Section I. See Sec. IV and Ref. [?] for the values obtained during the data run.

f_{lo}	4.707506 GHz
f_{hi}	4.798145 GHz
N_{step}	839
Δf_{step}	$95 - 115$ kHz
$f_{\mathrm{resolution}}$	1 kHz
B_0	8 Tesla
V	0.234 L
C_{010}	$0.64 - 0.69$
Q_0	$59000 - 65000$
β	$1.9 - 2.3$
T_{cavity}	155 mK
$\mathrm{T_A}$	$1.9 - 2.2$ K
$\Delta\nu_a$	5 kHz

that the HEMT performance was stable over time. The average of the added noise $\mathrm{T_A}$ over 19 measurements has the lowest value of 1.9 K at the frequency of 4.8 GHz and the highest value of 2.2 K at 4.72 GHz, as presented in Fig. 1. The error bars are the RMS of $\mathrm{T_A}$ and the largest RMS was used to calculate the systematic uncertainty for the limits on $g_{a\gamma\gamma}$. The light blue points in Fig. 1 are the noise from the axion data estimated by removing gain and subtracting the contribution from the cavity noise, assuming that the presence of a narrow signal in the data would have no effect on the estimation. A good agreement between the results from the HEMT calibration and the results estimated from the axion data is shown. The biggest difference is 0.076 K in the frequency range during which the data were recorded after an earthquake. The source of the difference is not understood, therefore, the difference is quoted as a systematic uncertainty together with the RMS of the noise.

FIG. 1. The average added noise from the HEMT calibration (pink points) and the noise estimated from the axion data (light blue points) as a function of frequency.

IV. ANALYSIS PROCEDURE

A. Analysis overview

Our goal is to find the axion signal hidden in the white noise. In order to achieve this, our analysis procedure includes the following steps:

1. Perform Fast Fourier transform (FFT) time-dependent spectrum to obtain the frequency-dependent spectrum.

2. Apply Savitzky-Golay (SG) filter to the oscillating structure of the frequency-dependent spectrum

3. Combine all power spectra from different frequency scans with weighting algorithm.

4. Merge bins in the combined spectrum to maximize the SNR.

5. Set limit on $g_{a\gamma\gamma}$.

The analysis was done by closely following the procedure from Haystac experiment [].

B. Fast Fourier transform

The time-dependent I and Q data were recorded and saved in TDMS (Technical Data Management Streaming) files - binary format developed by **National Instruments**). Fast Fourier Transform (FFT) was performed to convert the data into frequency-dependent and into unit of power by using the equation:

$$\text{Power} = \frac{|\text{FFT}(I + i \cdot Q)|^2}{N \cdot 2R} \tag{8}$$

where N is the number of data points ($N_A = 2000$ in our experiment), and R is the resistor of the signal analyzer (50 Ω).

10

C. Remove the oscillating structure

In case of absence axion signal, the output data is the noise of the cavity and the amplification chain. If axion presents in the cavity, its power will be buried in the noise because the signal is very weak. Therefore, the structure of the raw output power spectrum, as shown in Fig. ??, is the product of the noise and the gain of the system. The Savitzky Golay (SG) filter [?] was applied to remove the structure/background. The SG filter is a digital filter that can smooth data without distorting the signal tendency. The filter was performed by fitting adjacent points of successive sub-sets of data with a nth-order polynomial. The result depends on two parameters: the number of data points used for fitting, so-called the window width, and the order of the polynomial. If the window is too wide, the filter will not remove small structures and if it is too narrow, it may kill the signal. The window and order were first chosen during the data taking based on the structure of data and the ratio between raw data and the filter output. After data taking, the window and order were optimized by injecting axion signal on top of noise data and found that they were consistent with the first choice. After filtering, the normalized spectrum (Fig. [?]) was obtained by dividing the raw spectrum by the background - output of the SG filter - and subtract 1. Therefore, if the signal exists, the excess power will be above 0. Since we adjusted the resonant frequency of the cavity to scan the large range of signal and reduce the noise at overlapped region, we need to combine all the spectra of all scans to create one big spectrum. Before doing this, the normalized spectrum of each scan was rescaled by the system noise [detailed in Sec [?]] and the signal power with taking the cavity Lorentzian shape into account. The rescaled spectrum, shown in Fig. [], was computed with formula:

$$P_{ij}^{res} = \frac{k_B T_S \Delta\nu P_{ij}^{norm}}{P_{ij}^{signal} h} \tag{9}$$

and standard deviation of each bin is:

$$\sigma_{ij}^{res} = \frac{k_B T_S \Delta\nu \sigma_i^{norm}}{P_{ij}^{signal} h} \tag{10}$$

where T_S is the system noise including amplifier adding noise and cavity thermal noise, $\Delta\nu$ is the bin width of spectrum, P_{ij}^{signal} is the KSVZ axion signal power $h = \frac{1}{1+[2(\nu_{ij}-\nu_{ci})/\Delta\nu_i]}$ is Lorentzian shape of the cavity and σ_i^{norm} is the standard deviation of normalized spectrum ith.

11

If a signal appears in a certain frequency bin n^th, its expected power will be enhanced or reduced depending on the bin position due to the cavity's Lorentzian shape. The rescaling will take into account this effect.

FIG. 2. The simulation for testing the effect of SG filter.

FIG. 3. Weighed SNR

D. Combine spectra with weighting algorithm

The purpose of weighting algorithm is to add different spectra vertically, particularly for the frequency bins that appear in multiple spectra. Each spectrum in Fig.?? was collected with a different cavity resonance frequency. Therefore, if a signal appears in a certain frequency bin n^{th}, due to the difference in resonance frequency and Lorentzian shape, the expected signal power will be different in each spectrum i. The weighting algorithm is expected to take this into account with weight of each bin n of spectrum i defined in Eq.[?]. The weighted power $\delta_{weighted})_k$ and standard deviation $\sigma_{weighted})_k$ of each bin k in the combined spectrum are calculated using Eq.[?] and Eq.[?], respectively. The SNR is the ratio of $\delta_{com})_k$ and $\sigma_{com})_k$ as given in Eq. [?].

$$w_n{}^i = \frac{1}{(\sigma_n^i)^2} \tag{11}$$

$$(\delta_{com})_n = \frac{\sum_i^k \delta_n^i \cdot w_n{}^i}{\sum_i^k w_n{}^i} \tag{12}$$

$$(\sigma_{com})_n = \frac{\sqrt{\sum_i^k (\sigma_n^i \cdot w_n{}^i)^2}}{\sum_i^k w_n{}^i} \tag{13}$$

$$(SNR_{com})_n = \frac{(\delta_{com})_n}{(\sigma_{com})_n} = \frac{\sum_i^k \delta_n^i \cdot w_n{}^i}{\sqrt{\sum_i^k (\sigma_n^i \cdot w_n{}^i)^2}} \tag{14}$$

12

E. Merging bins

With the quality factor of 10^6, the expected axion bandwidth is of 5 kHz at frequency of 5 GHz. Our interested range is 4.7 - 4.8 GHz and the bin width is of 1 kHz. Therefore, in order to maximize the SNR without splitting the signal power in multiple successive bins in the final spectrum, we merged M = 5 bins with overlapping. Therefore, in order to maximize the SNR, we merged 5 consecutive bins with overlapping of the combined spectrum to construct a final spectrum. The purpose of overlapping is to avoid the signal power broken into different neighbouring bins of the merged spectrum. Before defining weights for merging, we multiplied the power and standard deviation of each bin in the combined spectrum by M: $\delta_n^{com} \to M\delta_n^{com}$ and $\sigma^{com})_n \to M\sigma^{com})_n$. This rescaling gives the expected mean of the normalized power $\mu_k^{comb} = 1$ if a KSVZ axion signal power leaves a fraction of 1/M of its power in the combined spectrum k. Then the maximum likelihood weights, defined in Eq. [?] based on the The Maxwellian lineshape for axion (Eq. []) used, were used to build the merged spectrum.

$$w_q = \frac{L_q}{(\sigma_q^{com}/5)^2} \tag{15}$$

$$L_q = \int_{\nu_a+\nu_q+(q+1)\Delta\nu}^{\nu_a+\nu_q+q\Delta\nu} f(\nu)\, d\nu \tag{16}$$

where L_q is the integral of the lineshape from the lower edge to higher edge of qth bin, $\sigma_q^{com})^2$ is the standard deviation of the combined spectrum as defined in Eq.[?]. The power, standard deviation and SNR of the merged spectrum are:

$$(\delta_{merged})_q = k \cdot \frac{\sum_{i=q-k/2}^{q+k/2}(\delta_{norm})_q^i/M \cdot w_q}{\sum_{i=q-k/2}^{q+k/2} w_q} \tag{17}$$

$$(\sigma_{merged})_q = k \cdot \frac{\sqrt{\sum_{i=q-k/2}^{q+k/2}((\sigma_{norm})_q^i/M)^2 \cdot (w_q)^2}}{\sum_{i=q-k/2}^{q+k/2} w_q} \tag{18}$$

$$(SNR_{merged})_q = \frac{(\delta_{merged})_q}{(\sigma_{merged})_q} = \frac{\sum_{i=q-k/2}^{q+k/2}(\delta_{norm})_q^i/M \cdot w_q}{\sqrt{\sum_{i=q-k/2}^{q+k/2}((\sigma_{norm})_q^i/M)^2 \cdot w_q^2}} \tag{19}$$

FIG. 4. The merged power δ following Eq.(17), standard deviation σ derived from Eq.(18), and signal to noise ratio SNR from Eq.(18)

FIG. 5. Our SNR target is 5σ, so if we want to have 95% of confidence, the threshold need to be 3.355σ $(5\sigma - 1.645\sigma)$.

V.   ANALYSIS OF THE SYNTHETIC AXION DATA

After TASEH finished collecting the CD102 data on November 15, 2021, the synthetic axion signals were injected into the cavity and read out via the same transmission line and amplification chain. The procedure to generate axion-like signals is summarized in Ref. [**?**]. Due to the uncertainties on the losses of readout electronics and transmission lines, the synthetic axion signals were not used to perform an absolute calibration of search sensitivity. Instead, a test with synthetic axion signals could be used to verify the procedures of data acquisition and physics analysis. The signal-to-noise ratio (SNR) of the frequency bin with maximum power, at 4.708972 GHz, was set to $\approx 3.35\sigma$, corresponding to a power of $\approx 6.03 \times 10^{-13}$ W in a 1-kHz frequency bin.

Figures 6–8 present respectively the power spectra in 24 frequency scans, the spectrum after combining the 24 spectra vertically, and the spectrum after merging five neighboring bins with a signal line shape following Eq. (4). Before combining the 24 spectra vertically, the SNR of the maximum-power bin from the spectrum with a cavity resonance frequency of 4.708918 GHz was measured to be 3.577σ; the SNR was slightly higher than 3.35σ due to a 5% difference in the noise fluctuation between the measurements from the HEMT calibration and the measurements taken right before injecting axion-like signals. After the vertical combination of power spectra and the merging of five frequency bins, the SNR increased to 4.74σ and 6.12σ, respectively. The analysis results of the synthetic axion signals proved that an power excess of more than 5σ can be found at the expected frequencies via the standard analysis procedure.

FIG. 6. The power spectra from the 24 frequency steps of the synthetic axion data. In order to show the spectra clearly, the spectra are shifted with respect to each other with an arbitrary offset in the vertical scale.

FIG. 7. The power spectrum after combining the spectra with overlapping frequencies vertically. The procedure and the weights for combination are summarized in Section IV.

FIG. 8. The power spectrum after merging the power measured in five neighboring frequency bins. The procedure and the weights for merging are summarized in Section IV.

VI.   SYSTEMATIC UNCERTAINTIES

The systematic uncertainties on the $g_{a\gamma\gamma}$ limits arise from the following sources:

- Uncertainty on the product $Q_L\beta/(1+\beta)$ in Eq. (2): In order to extract the loaded quality factor Q_L and the coupling parameter β, a fitting of the measured results of the cavity scattering matrix was performed, which results in a relative uncertainty of 0.2% on this product.

- Uncertainty on the noise temperature T_A from the RMS of the measurements in the HEMT calibration: $\Delta T_A/T_A = 2.3\%$ (see Section III and Fig. 1).

- Uncertainty on the noise temperature T_A from the largest difference between the value determined by the HEMT calibration and that from the axion data: $\Delta T_A/T_A = 4\%$ (see Section III and Fig. 1).

- Uncertainty from the choice of the SG-filter parameters: i.e. the window width and the order of the polynomial in the SG filter. Before collecting the axion data, a preliminary optimization was performed: a window width of 201 bins and a 4th order polynomial were used for the first analysis of the CD102 data (see Section IV). This choice was kept for the central results. Nevertheless, various methods of optimization were also explored. The methods include:

  - Minimize the difference between the two functions returned by the SG filter, with and without injecting a simulated axion signal to the real data.

  - Minimize the difference between the function returned by the SG filter and the input noise function by simulating both the noise spectrum (including the Lorentzian distribution due to the cavity noise) and the axion signal. See Fig. 9

15

for a comparison of the simulated spectrum, input noise function, and the function returned by the SG-filter when a 3$^{\text{rd}}$-order polynomial and a window of 141 bins are chosen; the differences from all the frequency bins are summed together when performing the optimization. Figure 10 shows the difference as a function of window widths when the order of polynomial is set to three, four, and six.

– Compare the mean μ_{noise} and the fluctuation of the measured power σ_{noise}, assuming no signal is present in the data. See Fig. 11 for an example distribution of the measured power from yyyyy bins when the cavity resonance frequency is set to xxx GHz; a Gaussian fit is performed to extract μ_{noise} and σ_{noise}. Given the nature of the thermal noise, the two variables are supposed to be related to each other if proper window width and order are chosen:

$$\sigma_{\text{noise}} = \frac{\mu_{\text{noise}}}{\sqrt{N_{\text{spectra}}}},$$

where N_{spectra} is the number of spectra for averaging and is related to the amount of integration time for each frequency step. In general, $N_{\text{spectra}} \approx xxxx$.

In addition, one could choose to optimize for each frequency step individually, optimize for a certain frequency step but apply the results to all data, or optimize by adding all the frequency steps together. Figure 12 shows that the deviations from the central results using different optimization approaches are in general within 1% and the maximum deviation of 1.8% on the $g_{a\gamma\gamma}$ limit is used as a conservative estimate of the systematic uncertainty from the SG filter.

The first source has negligible effect on the limits of $g_{a\gamma\gamma}$while the latter three sources are studied and added in quadrature to obtain the total systematic uncertainty.

FIG. 9. Upper panel: The simulated spectrum, including the axion signal and the noise from the cavity and the receiver chain, is overlaid with the input noise function and the function returned by the SG filter. Lower panel: The ratio of the function returned by the SG filter to the input noise function.

FIG. 10. The difference between the function returned by the SG filter and the input noise function, when various values of window widths and a 3rd, a 4th, or a 6th-order polynomial are applied in the SG filter. In this example, the best choice is a 4th-order polynomial with a window width of 241 data points (bins).

FIG. 11. An example of the distribution of the measured power when the cavity resonance frequency is xxxx GHz. The distribution contains xxxx entries and each entry corresponds to the measured power, averaged over yyy spectra, in one frequency bin. The mean and the width returned by a Gaussian fit to the distribution are used to determine the best choice of SG parameters.

VII. RESULTS

In Fig.5, we set a threshold at 3.355σ, if the expected signal is 5 σ above the noise level, the signal is supposed to have 95% of the chance passing the cut at 3.355 sigma. However, a signal was not observed. Therefore, with 95% C.L., the signal cannot be larger than 5 σ.

VIII. CONCLUSION

Appendix A: The derivation of the noise spectrum from the cavity

The Hamiltonian of a single-mode cavity is

$$H = \hbar\omega_{\mathrm{c}}(C^{\dagger}C + \frac{1}{2}), \tag{A1}$$

where $\omega_{\mathrm{c}}/2\pi$ is the cavity resonance frequency and C is the annihilation operator of the inner cavity field. The cavity field is coupled to the modes A of a transmission line with

FIG. 12. The ratio of the limits on $g_{a\gamma\gamma}$ due to the different choices of window width and order of polynomial in the SG filter, with respect to the central results (a window width of 201 bins and 4th-order polynomial).

FIG. 13. Set the limit with 5 σ

the rate κ_2. The cavity field is also coupled to the environment modes B with the rate κ_0. Based on the model of Fig. 14 and the input-output theory, the equation of motion for C is obtained:

$$\frac{dC}{dt} = -i\omega_c C - \frac{\kappa_2 + \kappa_0}{2}C + \sqrt{\kappa_2}A_{\text{in}} + \sqrt{\kappa_0}B_{\text{in}}. \tag{A2}$$

A boundary condition holds for the transmission modes:

$$A_{\text{out}} = \sqrt{\kappa_2}C - A_{\text{in}}. \tag{A3}$$

Considering working in a rotating frame of the signal frequency ω near ω_c, the equation of motion becomes:

$$-i\omega C + \frac{dC}{dt} = -i\omega_c C - \frac{\kappa_2 + \kappa_0}{2}C + \sqrt{\kappa_2}A_{\text{in}} + \sqrt{\kappa_0}B_{\text{in}}. \tag{A4}$$

The steady state solution for the cavity field is:

$$C = \frac{\sqrt{\kappa_2}A_{\text{in}} + \sqrt{\kappa_0}B_{\text{in}}}{-i(\omega - \omega_c) + \frac{\kappa_2 + \kappa_0}{2}}. \tag{A5}$$

By substituting Eq. (A5) into Eq. (A3), the reflected modes of the transmission line A_{out} are expressed in terms of the input modes of the transmission line A_{in} and the environment B_{in}:

$$\begin{aligned}
A_{\text{out}} &= \frac{i(\omega - \omega_c) + \frac{\kappa_2 - \kappa_0}{2}}{-i(\omega - \omega_c) + \frac{\kappa_2 + \kappa_0}{2}}A_{\text{in}} + \frac{\sqrt{\kappa_2 \kappa_0}}{-i(\omega - \omega_c) + \frac{\kappa_2 + \kappa_0}{2}}B_{\text{in}} \\
&= \frac{-(\omega - \omega_c)^2 + \frac{\kappa_2^2 - \kappa_0^2}{4} + i\kappa_2(\omega - \omega_c)}{(\omega - \omega_c)^2 + (\frac{\kappa_2 + \kappa_0}{2})^2}A_{\text{in}} + \frac{\sqrt{\kappa_2 \kappa_0}\frac{\kappa_2 + \kappa_0}{2} + i\sqrt{\kappa_2 \kappa_0}(\omega - \omega_c)}{(\omega - \omega_c)^2 + (\frac{\kappa_2 + \kappa_0}{2})^2}B_{\text{in}}.
\end{aligned} \tag{A6}$$

Therefore, the autocorrelation of A_{out} is related to those of A_{in} and B_{in}:

$$\begin{aligned}
\langle A_{\text{out}}^\dagger A_{\text{out}}\rangle &= \frac{[(\omega - \omega_c)^2 - \frac{\kappa_2^2 - \kappa_0^2}{4}]^2 + \kappa_2^2(\omega - \omega_c)^2}{[(\omega - \omega_c)^2 + (\frac{\kappa_2 + \kappa_0}{2})^2]^2}\langle A_{\text{in}}^\dagger A_{\text{in}}\rangle \\
&\quad + \frac{\kappa_2 \kappa_0(\frac{\kappa_2 + \kappa_0}{2})^2 + \kappa_2 \kappa_0(\omega - \omega_c)^2}{[(\omega - \omega_c)^2 + (\frac{\kappa_2 + \kappa_0}{2})^2]^2}\langle B_{\text{in}}^\dagger B_{\text{in}}\rangle.
\end{aligned} \tag{A7}$$

The spectrum from the cavity $S(\omega)$ is found to be related to the spectrum of the readout transmission line $S_{\text{rt}}(\omega)$ and the spectrum of the cavity environment $S_{\text{cav}}(\omega)$:

$$\begin{aligned}
S(\omega) &= \frac{[(\omega - \omega_c)^2 - \frac{\kappa_2^2 - \kappa_0^2}{4}]^2 + \kappa_2^2(\omega - \omega_c)^2}{[(\omega - \omega_c)^2 + (\frac{\kappa_2 + \kappa_0}{2})^2]^2}S_{\text{rt}}(\omega) \\
&\quad + \frac{\kappa_2 \kappa_0(\frac{\kappa_2 + \kappa_0}{2})^2 + \kappa_2 \kappa_0(\omega - \omega_c)^2}{[(\omega - \omega_c)^2 + (\frac{\kappa_2 + \kappa_0}{2})^2]^2}S_{\text{cav}}(\omega).
\end{aligned} \tag{A8}$$

18

As the the readout transmission line and the cavity environment are both in thermal states, i.e. $S_{\mathrm{rt}}(\omega) = [n_{\mathrm{BE}}(T_{\mathrm{rt}}) + 1/2]\,\hbar\omega$ and $S_{\mathrm{cav}}(\omega) = [n_{\mathrm{BE}}(T_{\mathrm{cav}}) + 1/2]\,\hbar\omega$, where n_{BE} is the mean photon number given by the Bose-Einstein distribution, $S(\omega)$ is white if $T_{\mathrm{cav}} = T_{\mathrm{rt}}$, and Lorentzian if $T_{\mathrm{cav}} \gg T_{\mathrm{rt}}$.
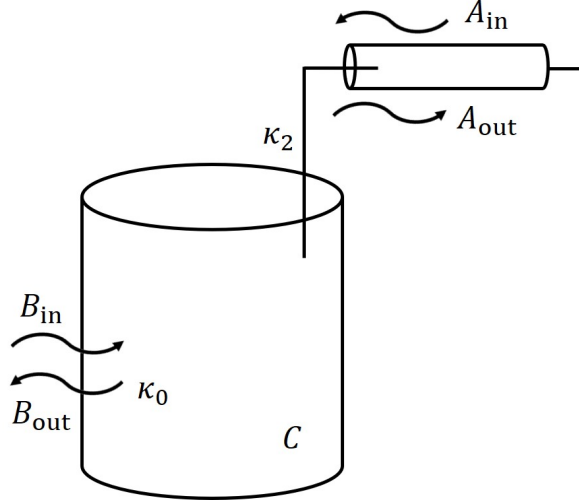
FIG. 14. A cavity is coupled to the modes of transmission line A with the rate κ_2 and the modes of environment B with the rate κ_0.

[1] R. D. Peccei and H. R. Quinn, CP conservation in the presence of pseudoparticles, Phys. Rev. Lett. **38**, 1440 (1977).

[2] S. Weinberg, A new light boson?, Phys. Rev. Lett. **40**, 223 (1978).

[3] F. Wilczek, Problem of strong p and t invariance in the presence of instantons, Phys. Rev. Lett. **40**, 279 (1978).

[4] C. Abel *et al.* (nEDM), Measurement of the permanent electric dipole moment of the neutron, Phys. Rev. Lett. **124**, 081803 (2020), arXiv:2001.11966 [hep-ex].

[5] P. D. Group, P. A. Zyla, R. M. Barnett, J. Beringer, O. Dahl, D. A. Dwyer, D. E. Groom, C. J. Lin, K. S. Lugovsky, E. Pianori, D. J. Robinson, C. G. Wohl, W. M. Yao, K. Agashe, G. Aielli, B. C. Allanach, C. Amsler, M. Antonelli, E. C. Aschenauer, D. M. Asner, H. Baer, S. Banerjee, L. Baudis, C. W. Bauer, J. J. Beatty, V. I. Belousov, S. Bethke, A. Bettini, O. Biebel, K. M. Black, E. Blucher, O. Buchmuller, V. Burkert, M. A. Bychkov, R. N. Cahn, M. Carena, A. Cec-

19

cucci, A. Cerri, D. Chakraborty, R. S. Chivukula, G. Cowan, G. D'Ambrosio, T. Damour, D. de Florian, A. de Gouvêa, T. DeGrand, P. de Jong, G. Dissertori, B. A. Dobrescu, M. D'Onofrio, M. Doser, M. Drees, H. K. Dreiner, P. Eerola, U. Egede, S. Eidelman, J. Ellis, J. Erler, V. V. Ezhela, W. Fetscher, B. D. Fields, B. Foster, A. Freitas, H. Gallagher, L. Garren, H. J. Gerber, G. Gerbier, T. Gershon, Y. Gershtein, T. Gherghetta, A. A. Godizov, M. C. Gonzalez-Garcia, M. Goodman, C. Grab, A. V. Gritsan, C. Grojean, M. Grünewald, A. Gurtu, T. Gutsche, H. E. Haber, C. Hanhart, S. Hashimoto, Y. Hayato, A. Hebecker, S. Heinemeyer, B. Heltsley, J. J. Hernández-Rey, K. Hikasa, J. Hisano, A. Höcker, J. Holder, A. Holtkamp, J. Huston, T. Hyodo, K. F. Johnson, M. Kado, M. Karliner, U. F. Katz, M. Kenzie, V. A. Khoze, S. R. Klein, E. Klempt, R. V. Kowalewski, F. Krauss, M. Kreps, B. Krusche, Y. Kwon, O. Lahav, J. Laiho, L. P. Lellouch, J. Lesgourgues, A. R. Liddle, Z. Ligeti, C. Lippmann, T. M. Liss, L. Littenberg, C. Lourengo, S. B. Lugovsky, A. Lusiani, Y. Makida, F. Maltoni, T. Mannel, A. V. Manohar, W. J. Marciano, A. Masoni, J. Matthews, U. G. Meißner, M. Mikhasenko, D. J. Miller, D. Milstead, R. E. Mitchell, K. Mönig, P. Molaro, F. Moortgat, M. Moskovic, K. Nakamura, M. Narain, P. Nason, S. Navas, M. Neubert, P. Nevski, Y. Nir, K. A. Olive, C. Patrignani, J. A. Peacock, S. T. Petcov, V. A. Petrov, A. Pich, A. Piepke, A. Pomarol, S. Profumo, A. Quadt, K. Rabbertz, J. Rademacker, G. Raffelt, H. Ramani, M. Ramsey-Musolf, B. N. Ratcliff, P. Richardson, A. Ringwald, S. Roesler, S. Rolli, A. Romaniouk, L. J. Rosenberg, J. L. Rosner, G. Rybka, M. Ryskin, R. A. Ryutin, Y. Sakai, G. P. Salam, S. Sarkar, F. Sauli, O. Schneider, K. Scholberg, A. J. Schwartz, J. Schwiening, D. Scott, V. Sharma, S. R. Sharpe, T. Shutt, M. Silari, T. Sjöstrand, P. Skands, T. Skwarnicki, G. F. Smoot, A. Soffer, M. S. Sozzi, S. Spanier, C. Spiering, A. Stahl, S. L. Stone, Y. Sumino, T. Sumiyoshi, M. J. Syphers, F. Takahashi, M. Tanabashi, J. Tanaka, M. Taševský, K. Terashi, J. Terning, U. Thoma, R. S. Thorne, L. Tiator, M. Titov, N. P. Tkachenko, D. R. Tovey, K. Trabelsi, P. Urquijo, G. Valencia, R. Van de Water, N. Varelas, G. Venanzoni, L. Verde, M. G. Vincter, P. Vogel, W. Vogelsang, A. Vogt, V. Vorobyev, S. P. Wakely, W. Walkowiak, C. W. Walter, D. Wands, M. O. Wascko, D. H. Weinberg, E. J. Weinberg, M. White, L. R. Wiencke, S. Willocq, C. L. Woody, R. L. Workman, M. Yokoyama, R. Yoshida, G. Zanderighi, G. P. Zeller, O. V. Zenin, R. Y. Zhu, S. L. Zhu, F. Zimmermann, J. Anderson, T. Basaglia, V. S. Lugovsky, P. Schaffner, and W. Zheng, Review of Particle Physics, Progress of Theoretical and Experimental Physics **2020**, 10.1093/ptep/ptaa104 (2020),

457 083C01, https://academic.oup.com/ptep/article-pdf/2020/8/083C01/34673722/ptaa104.pdf.

[6] S. Borsanyi *et al.*, Calculation of the axion mass based on high-temperature lattice quantum chromodynamics, Nature **539**, 69 (2016), arXiv:1606.07494 [hep-lat].

[7] M. Dine, P. Draper, L. Stephenson-Haskins, and D. Xu, Axions, Instantons, and the Lattice, Phys. Rev. D **96**, 095001 (2017), arXiv:1705.00676 [hep-ph].

[8] T. Hiramatsu, M. Kawasaki, T. Sekiguchi, M. Yamaguchi, and J. Yokoyama, Improved estimation of radiated axions from cosmological axionic strings, Phys. Rev. D **83**, 123531 (2011), arXiv:1012.5502 [hep-ph].

[9] M. Kawasaki, K. Saikawa, and T. Sekiguchi, Axion dark matter from topological defects, Phys. Rev. D **91**, 065014 (2015), arXiv:1412.0789 [hep-ph].

[10] E. Berkowitz, M. I. Buchoff, and E. Rinaldi, Lattice QCD input for axion cosmology, Phys. Rev. D **92**, 034507 (2015), arXiv:1505.07455 [hep-ph].

[11] L. Fleury and G. D. Moore, Axion dark matter: strings and their cores, JCAP **01**, 004, arXiv:1509.00026 [hep-ph].

[12] C. Bonati, M. D'Elia, M. Mariti, G. Martinelli, M. Mesiti, F. Negro, F. Sanfilippo, and G. Villadoro, Axion phenomenology and θ-dependence from $N_f = 2 + 1$ lattice QCD, JHEP **03**, 155, arXiv:1512.06746 [hep-lat].

[13] P. Petreczky, H.-P. Schadler, and S. Sharma, The topological susceptibility in finite temperature QCD and axion cosmology, Phys. Lett. B **762**, 498 (2016), arXiv:1606.03145 [hep-lat].

[14] G. Ballesteros, J. Redondo, A. Ringwald, and C. Tamarit, Unifying inflation with the axion, dark matter, baryogenesis and the seesaw mechanism, Phys. Rev. Lett. **118**, 071802 (2017), arXiv:1608.05414 [hep-ph].

[15] V. B. . Klaer and G. D. Moore, The dark-matter axion mass, JCAP **11**, 049, arXiv:1708.07521 [hep-ph].

[16] M. Buschmann, J. W. Foster, and B. R. Safdi, Early-Universe Simulations of the Cosmological Axion, Phys. Rev. Lett. **124**, 161103 (2020), arXiv:1906.00967 [astro-ph.CO].

[17] M. Gorghetto, E. Hardy, and G. Villadoro, More axions from strings, SciPost Phys. **10**, 050 (2021), arXiv:2007.04990 [hep-ph].

[18] M. Buschmann, J. W. Foster, A. Hook, A. Peterson, D. E. Willcox, W. Zhang, and B. R. Safdi, Dark Matter from Axion Strings with Adaptive Mesh Refinement, (2021), arXiv:2108.05368 [hep-ph].

[19] P. Sikivie and Q. Yang, Bose-einstein condensation of dark matter axions, Phys. Rev. Lett. **103**, 111301 (2009).

[20] P. Sikivie, The emerging case for axion dark matter, Physics Letters B **695**, 22 (2011).

[21] N. Banik and P. Sikivie, Axions and the galactic angular momentum distribution, Phys. Rev. D **88**, 123517 (2013).

[22] J. E. Kim, Weak Interaction Singlet and Strong CP Invariance, Phys. Rev. Lett. **43**, 103 (1979).

[23] M. A. Shifman, A. I. Vainshtein, and V. I. Zakharov, Can Confinement Ensure Natural CP Invariance of Strong Interactions?, Nucl. Phys. B **166**, 493 (1980).

[24] M. Dine, W. Fischler, and M. Srednicki, A Simple Solution to the Strong CP Problem with a Harmless Axion, Phys. Lett. B **104**, 199 (1981).

[25] A. R. Zhitnitsky, On Possible Suppression of the Axion Hadron Interactions. (In Russian), Sov. J. Nucl. Phys. **31**, 260 (1980).

[26] P. Sikivie, Experimental tests of the "invisible" axion, Phys. Rev. Lett. **51**, 1415 (1983).

[27] P. Sikivie, Detection rates for "invisible"-axion searches, Phys. Rev. D **32**, 2988 (1985).

[28] C. Hagmann, D. Kinion, W. Stoeffl, K. van Bibber, E. Daw, H. Peng, L. J. Rosenberg, J. LaVeigne, P. Sikivie, N. S. Sullivan, D. B. Tanner, F. Nezrick, M. S. Turner, D. M. Moltz, J. Powell, and N. A. Golubev, Results from a high-sensitivity search for cosmic axions, Phys. Rev. Lett. **80**, 2043 (1998).

[29] S. J. Asztalos, E. Daw, H. Peng, L. J. Rosenberg, D. B. Yu, C. Hagmann, D. Kinion, W. Stoeffl, K. van Bibber, J. LaVeigne, P. Sikivie, N. S. Sullivan, D. B. Tanner, F. Nezrick, and D. M. Moltz, Experimental constraints on the axion dark matter halo density, The Astrophysical Journal **571**, L27 (2002).

[30] S. J. Asztalos, R. F. Bradley, L. Duffy, C. Hagmann, D. Kinion, D. M. Moltz, L. J. Rosenberg, P. Sikivie, W. Stoeffl, N. S. Sullivan, D. B. Tanner, K. van Bibber, and D. B. Yu, Improved rf cavity search for halo axions, Phys. Rev. D **69**, 011101 (2004).

[31] S. J. Asztalos, G. Carosi, C. Hagmann, D. Kinion, K. van Bibber, M. Hotz, L. J. Rosenberg, G. Rybka, J. Hoskins, J. Hwang, P. Sikivie, D. B. Tanner, R. Bradley, and J. Clarke, Squid-based microwave cavity search for dark-matter axions, Phys. Rev. Lett. **104**, 041301 (2010).

[32] N. Du, N. Force, R. Khatiwada, E. Lentz, R. Ottens, L. J. Rosenberg, G. Rybka, G. Carosi, N. Woollett, D. Bowring, A. S. Chou, A. Sonnenschein, W. Wester, C. Boutan, N. S. Oblath,

R. Bradley, E. J. Daw, A. V. Dixit, J. Clarke, S. R. O'Kelley, N. Crisosto, J. R. Gleason, S. Jois, P. Sikivie, I. Stern, N. S. Sullivan, D. B. Tanner, and G. C. Hilton (ADMX Collaboration), Search for invisible axion dark matter with the axion dark matter experiment, Phys. Rev. Lett. **120**, 151301 (2018).

[33] T. Braine, R. Cervantes, N. Crisosto, N. Du, S. Kimes, L. J. Rosenberg, G. Rybka, J. Yang, D. Bowring, A. S. Chou, R. Khatiwada, A. Sonnenschein, W. Wester, G. Carosi, N. Woollett, L. D. Duffy, R. Bradley, C. Boutan, M. Jones, B. H. LaRoque, N. S. Oblath, M. S. Taubman, J. Clarke, A. Dove, A. Eddins, S. R. O'Kelley, S. Nawaz, I. Siddiqi, N. Stevenson, A. Agrawal, A. V. Dixit, J. R. Gleason, S. Jois, P. Sikivie, J. A. Solomon, N. S. Sullivan, D. B. Tanner, E. Lentz, E. J. Daw, J. H. Buckley, P. M. Harrington, E. A. Henriksen, and K. W. Murch (ADMX Collaboration), Extended search for the invisible axion with the axion dark matter experiment, Phys. Rev. Lett. **124**, 101303 (2020).

[34] A. Collaboration, C. Bartram, T. Braine, E. Burns, R. Cervantes, N. Crisosto, N. Du, H. Korandla, G. Leum, P. Mohapatra, T. Nitta, L. J. Rosenberg, G. Rybka, J. Yang, J. Clarke, I. Siddiqi, A. Agrawal, A. V. Dixit, M. H. Awida, A. S. Chou, M. Hollister, S. Knirck, A. Sonnenschein, W. Wester, J. R. Gleason, A. T. Hipp, S. Jois, P. Sikivie, N. S. Sullivan, D. B. Tanner, E. Lentz, R. Khatiwada, G. Carosi, N. Robertson, N. Woollett, L. D. Duffy, C. Boutan, M. Jones, B. H. LaRoque, N. S. Oblath, M. S. Taubman, E. J. Daw, M. G. Perry, J. H. Buckley, C. Gaikwad, J. Hoffman, K. W. Murch, M. Goryachev, B. T. McAllister, A. Quiskamp, C. Thomson, and M. E. Tobar, Search for "invisible" axion dark matter in the 3.3-4.2 μev mass range (2021), arXiv:2110.06096 [hep-ex].

[35] K. M. Backes, D. A. Palken, S. A. Kenany, B. M. Brubaker, S. B. Cahn, A. Droster, G. C. Hilton, S. Ghosh, H. Jackson, S. K. Lamoreaux, and et al., A quantum enhanced search for dark matter axions, Nature **590**, 238–242 (2021).

[36] O. Kwon, D. Lee, W. Chung, D. Ahn, H. Byun, F. Caspers, H. Choi, J. Choi, Y. Chong, H. Jeong, J. Jeong, J. E. Kim, J. Kim, i. m. c. b. u. Kutlu, J. Lee, M. Lee, S. Lee, A. Matlashov, S. Oh, S. Park, S. Uchaikin, S. Youn, and Y. K. Semertzidis, First results from an axion haloscope at capp around 10.7 μeV, Phys. Rev. Lett. **126**, 191802 (2021).

[37] M. S. Turner, Periodic signatures for the detection of cosmic axions, Phys. Rev. D **42**, 3572 (1990).

[38] M. Lisanti, Lectures on Dark Matter Physics, in *Theoretical Advanced Study Institute in*

Elementary Particle Physics: New Frontiers in Fields and Strings (2017) pp. 399–446, arXiv:1603.03797 [hep-ph].

[39] J. Diemand, M. Kuhlen, P. Madau, M. Zemp, B. Moore, D. Potter, and J. Stadel, Clumps and streams in the local dark matter distribution, Nature **454**, 735 (2008), arXiv:0805.1244 [astro-ph].

[40] V. Springel, J. Wang, M. Vogelsberger, A. Ludlow, A. Jenkins, A. Helmi, J. F. Navarro, C. S. Frenk, and S. D. M. White, The Aquarius Project: the subhalos of galactic halos, Mon. Not. Roy. Astron. Soc. **391**, 1685 (2008), arXiv:0809.0898 [astro-ph].

[41] J. F. Navarro, C. S. Frenk, and S. D. M. White, The Structure of cold dark matter halos, Astrophys. J. **462**, 563 (1996), arXiv:astro-ph/9508025.

[42] A. Burkert, The Structure of dark matter halos in dwarf galaxies, Astrophys. J. Lett. **447**, L25 (1995), arXiv:astro-ph/9504041.

[43] G. R. Blumenthal, S. M. Faber, R. Flores, and J. R. Primack, Contraction of Dark Matter Galactic Halos Due to Baryonic Infall, Astrophys. J. **301**, 27 (1986).

[44] O. Y. Gnedin, A. V. Kravtsov, A. A. Klypin, and D. Nagai, Response of dark matter halos to condensation of baryons: Cosmological simulations and improved adiabatic contraction model, Astrophys. J. **616**, 16 (2004), arXiv:astro-ph/0406247.

[45] S. Mashchenko, J. Wadsley, and H. M. P. Couchman, Stellar Feedback in Dwarf Galaxy Formation, Science **319**, 174 (2008), arXiv:0711.4803 [astro-ph].

[46] F. Governato *et al.*, At the heart of the matter: the origin of bulgeless dwarf galaxies and Dark Matter cores, Nature **463**, 203 (2010), arXiv:0911.2237 [astro-ph.CO].